Materials Research Express

PAPER

Structural characterizations of pure SnS and In-doped SnS thin films using isotropic and anisotropic models

RECEIVED
13 February 2018

REVISED
24 March 2018

ACCEPTED FOR PUBLICATION
12 April 2018

PUBLISHED
27 April 2018

Hosein Kafashan

Department of Materials Science and Engineering, Ahvaz Branch, Islamic Azad University, Ahvaz, Iran

E-mail: hosein840521@gmail.com **and** hosein.kafashan@iauahvaz.ac.ir

Keywords: SnS, electrodeposition, Williamson-Hall, X-ray, In-doping, size-strain plot

Abstract

An electrochemical route has been employed to prepare pure SnS and indium-doped SnS thin films. Six samples including undoped SnS and In-doped SnS thin films deposited on the fluorine-doped tin oxide (FTO) glass substrates. An aqueous solution having $SnCl_2$ and $Na_2S_2O_3$ used as the primary electrolyte. Different In-doped SnS samples were prepared by adding a different amount of 1 mM $InCl_3$ solution into the first electrolyte. The applied potential (E), time of deposition (t), pH and bath temperature (T) were kept at −1 V, 30 min, 2.1 and 60 °C, respectively. For all samples, except the In-dopant concentration, all the deposition parameters are the same. After preparation, X-ray diffraction (XRD), field emission scanning electron microscopy (FESEM) with an energy dispersive X-ray analyzer (EDX) attachment, atomic force microscopy (AFM), and transmission electron microscopy (TEM) were used to determine structural properties of as-deposited films. XRD patterns revealed that the synthesized undoped- and In-doped SnS thin films were crystallized in the orthorhombic structure. The shape of SnS crystals was spherical in the TEM image. X-ray peak broadening studies was done by applying Scherrer's method, Williamson-Hall (W–H) models (including uniform deformation model (UDM), uniform strain deformation model (UDSM), and uniform deformation energy density model (UDEDM)), and size-strain plot (SSP) method. Using these techniques, the crystallite size and the lattice strains have been predicted. There was a good agreement in the particle size achieved by W–H- and SSP methods with TEM image.

1. Introduction

In recent years, tin sulfide (SnS) has attracted much attention, with an extensive range of applications such as in near-infrared detectors, electrochemical capacitors [1], holographic recording, photovoltaic cells, and lithium-ion batteries, [2–8]. SnS is a semiconductor belongs to the IV–VI group, which it has a long b-axis with lattice constants of a = 0.4321 nm, b = 1.119 23 nm, and c = 0.398 38 nm [9]. It has a layered structure. According to figure 1, SnS consists of two weakly van der Waals force bonded layers, in which atoms are tightly bonded with covalence bond. SnS has a variety of energy band gap which related to the preparation method. The band gap of SnS has been reported as 1.3–2.3 eV for direct band gap and 1.0–1.2 eV for indirect band gap [10]. Because of the unique features of SnS such as high absorption coefficient ($>10^4$ cm^{-1}) [11], suitable carrier concentration [9], plentiful in nature, non-toxicity, and cost efficiency, it was a promising candidate for use in absorber layers in thin film solar cell applications.

Various techniques were used to deposit SnS such as spray pyrolytic-deposition [12–14], molecular beam epitaxy (MBE) [15], hydrothermal method [6, 7, 16], chemical bath deposition [17–20], electron beam evaporation [21, 22], SILAR method [23], and electrodeposition technique [11, 24]. The electrochemical route is a good method due to simplicity, cost-efficiency, and the facility of controlling its parameters with high accuracy. Also, this method is inexpensive [25].

To estimate the crystallite size of material, the Scherrer's method has been applied. Nevertheless, two essential factors including inhomogeneous strain and instrumental effects have not taken into account for

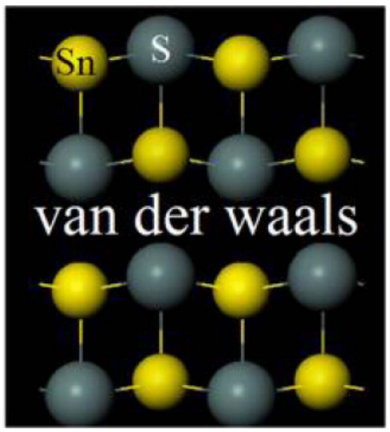

Figure 1. The arrangement of Sn and S in the SnS lattice.

acquiring crystallite size. Therefore, the W–H and SSP methods are an average technique to a much realistic estimation of the crystallite size and lattice strain [26]. As we know, the diffraction peaks will be broadened due to the deviation from perfect crystallinity. From peak width analysis, it can be obtained the crystallite size and lattice strain. The particle size is almost bigger than crystallite size due to the aggregation of crystallite structures [27]. In order to a real crystal deviate from a perfect crystal, the lattice strain has been created. The sources of lattice strain are crystalline defects such as dislocations, grain boundaries, triple junctions, sinter stresses, stacking faults, coherency stresses, etc. Some structural parameters such as the breath of peaks, the peaks intensity and the peak position shifts impacted on crystallite size and lattice strain. The peak width and the lattice strain depended on the $1/\cos\theta$ and $\tan\theta$, respectively [28]. In order to obtain the crystallite size and lattice strain as a function of 2θ, it can be used by two methods named Williamson-Hall (W–H)- and the size-strain plot (SSP) methods.

In this work, six samples (containing undoped SnS and In-doped SnS) have been synthesized by electrochemical deposition from an aqueous solution. With the use of XRD data, the crystallite size, the lattice strain, and the other associated parameters have been achieved by UDM, UDSM, UDEDM, and the SSP methods. The crystallite size values acquired from Scherrer's method, W–H, and SSP methods confirmed by TEM image. We found that the W–H and SSP methods have not yet been investigated on the In-doped SnS thin films.

2. Experimental

2.1. Materials and processing

Pure and In-doped SnS thin films deposited using an electrochemical route on fluorine-doped tin oxide (FTO) coated glass substrate. The effective surface area of FTO substrates (used as working electrode) was 1 cm $\times$ 1 cm. A platinum sheet and a saturated calomel electrode (SCE) were used as the anode and the reference electrode, respectively. The electrolyte was an aqueous solution of $SnCl_2$ (2 mM) and $Na_2S_2O_3$ (16 mM), and $InCl_3$ (1 mM) aqueous solution supplied the In-dopant. By adding diluted H_2SO_4, the pH of solution reduced from 3.8 to 2.1. Before the deposition process, the FTO and the platinum sheet cleaned and then rinsed with ethanol/acetone and distilled water. The temperature of the bath was 60 °C. The deposition process was done during 30 min. In addition, by a computer-controlled electrochemical analyzer (potentiostat, Autolab, A3ut71167, Netherlands), the applied deposition potential kept constant at −1 V. After the deposition process, the substrates were taken out from the bath and washed with distilled water. Following relation shows the mechanism of the formation of SnS on cathode electrode,

$$\begin{aligned} Sn^{2+} + 2e^- &\rightarrow Sn \\ S_2O_3{}^{2-} + 2H^+ &\rightarrow S + H_2SO_3 \\ Sn^{2+} + S + 2e^- &\rightarrow SnS \end{aligned} \quad (1)$$

According to the above reactions, the $Na_2S_2O_3$ is unstable in acidic media. Therefore, it is easy to separate the sulfur, and consequently, the Sn^{2+} and S reduced at the cathode (substrate) to form SnS. In this study, pure SnS and In-doped SnS thin films were prepared using electrodeposition method. The undoped SnS named as I (0), and the In-doped SnS thin films named as I (1)–I (5). Using EDX analysis, the atomic percentage of In-dopant in I (1), I (2), I (3), I (4), and I (5) samples obtained 1.30, 2.13, 2.59, 2.90, and 3.58%, respectively.

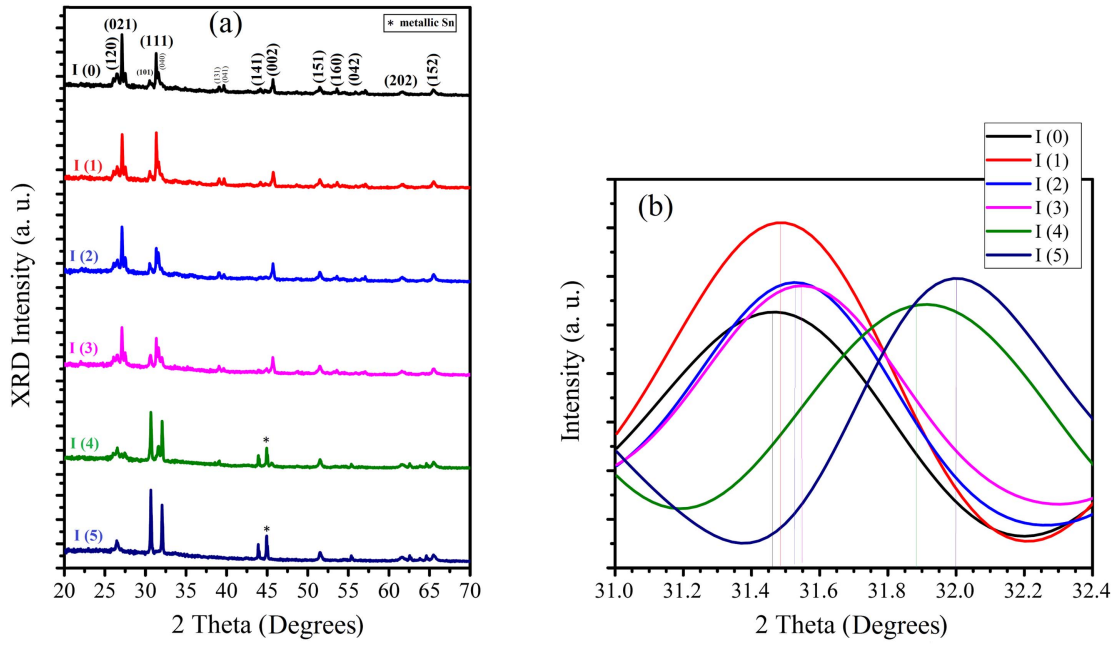

Figure 2. (a) X-ray diffraction patterns of In-doped SnS thin films and (b) the X-ray diffraction for (111) plane [29].

2.2. Characterization of the films

In order to inspect the type of phases of the deposited samples, a Philips X'Pert-MPD x-ray diffraction diffractometer (XRD) system with Cu-Kα radiation has been employed. Elemental analysis was achieved by a TE-SCAN field emission scanning electron microscopy (FESEM) with an energy dispersive X-ray analyzer (EDX) attachment. The topography of the deposited samples checked by atomic force microscopy (AFM- ARA AFM). A PHILIPS CM120 TEM was used to study the shape and the size of SnS particles. Varian-Cary Eclipse room temperature photoluminescence (PL) was employed to analyze the optical characterization of nanostructured SnS samples.

3. Results and discussion

3.1. XRD analysis

X-ray diffraction (XRD) test is a robust nondestructive method that used for characterizing the structural phases of various compounds. Therefore, XRD is a unique method in determination of crystallinity of a compound. Figure 2(a) depicted the XRD patterns of deposited samples. The crystalline structure of all deposited films was orthorhombic SnS with JCPDS 039-0354. As it was evident in this figure, the I (0), I (1), I (2), and I (3) samples were grown along (021) and (111), and the I (4) and I (5) samples were grown along (101) and (040). Therefore, it is interesting that the change in the preferential orientation of as-deposited In-doped SnS thin films was observed due to increment in In-dopant concentration. Also, no trace of In, In_2O_3, and In_2S_3 or other impurities cannot be detected in all samples. As it is observed in XRD patterns, with an increase in In-dopant concentration, the peaks will become less intense and broader, which indicating a decrease in crystallinity of samples. Hence, it shows a significant increase in crystalline defects and mismatching due to In-doping.

To better examine the influence of indium-doping on the structural properties of SnS, the plot of I-2 θ for (111) plane diffraction peak (figure 2(b)) of all samples has been drawn. A shift of (111) peak position to higher 2 θ has been detected due to the variation in the effective ionic radii between Sn^{2+} (0.93 A) and In^{3+} (0.80 A).

The lattice constants for pure SnS and In-doped SnS thin films can be obtained from the following relation [30],

$$\frac{1}{d_{hkl}^2} = \frac{h^2}{a^2} + \frac{k^2}{b^2} + \frac{l^2}{c^2} \tag{2}$$

where (hkl) is the Miller indices for the planes with the most intensity, i.e. (040), (021), (111) planes, and the d_{hkl} is the inter-planar distance. Table 1 summarized the calculated lattice parameters and structural parameters for pure SnS and In-doped SnS samples. It is clear that the substitution of In^{3+} for Sn^{2+} in SnS structure leads to a reduction in the unit cell volume. The reason for this phenomenon is the smaller effective ionic radii of In^{3+} compared with Sn^{2+}, which it caused a decrease in the d_{hkl} and consequently unit cell volume. The effect of In-

Table 1. Some structural properties of pure SnS and In-doped SnS samples originated from XRD patterns.

Sample	2θ	FWHM $\times 10^4$ rad	Average FWHM $\times 10^4$ rad	d_{hkl} ($\AA$)	Lattice Parameters ($\AA$)			V $\AA^3$
					a	b	c	
I (0)	27.090	19.89	20.24	3.288 52	4.319 194	11.323 48	4.039 835	197.581
	31.305	16.40		2.8550 9				
	31.579	24.43		2.830 87				
I (1)	27.113	19.37	22.57	3.289 36	4.313 475	11.323 72	4.039 55	197.310
	31.330	16.92		2.853 07				
	31.604	31.41		2.830 49				
I (2)	27.095	21.29	22.92	3.288 39	4.310 066	11.321 96	4.041 669	197.227
	31.324	16.05		2.853 34				
	31.579	31.41		2.830 93				
I (3)	27.086	20.76	24.55	3.286 16	4.315 423	11.314 88	4.037 021	197.121
	31.327	16.23		2.852 87				
	31.584	36.65		2.828 72				
I (4)	27.060	38.39	27.10	3.281 21	4.259 288	11.166 12	3.997 455	190.117
	30.655	19.89		2.761 53				
	32.044	23.03		2.914 13				
I (5)	26.489	36.65	25.59	3.292 69	4.258 984	11.163 56	3.997 169	190.047
	30.654	19.19		2.830 99				
	32.036	20.94		2.790 89				

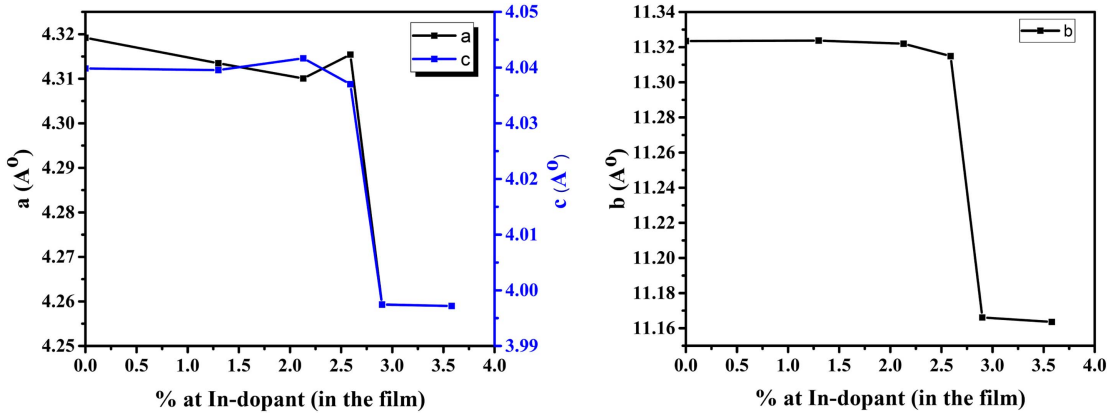

Figure 3. The variation in the lattice parameters of pure SnS and In-doped SnS thin films.

doping on the lattice parameters of SnS thin films shows in figure 3. As it was apparent in this figure, the lattice parameters of SnS thin films has been increased due to In-doping. This occurrence clearly indicates that the In-dopant is substitutionally doped into SnS lattice.

Using atomic force microscopy (AFM), the topographical examinations of I (0), I (1), and I (2) samples was done over an area of 6 μm $\times$ 6 μm. Figure 4 displays the AFM images of the as-deposited films. Figure 4 showed that an increase in the amount of In-dopant in SnS lattice leads to change in the morphology from grain-like to columnar growth thin planes. In addition, the grain size of SnS thin films became finer due to In-doping. Therefore, the variation in the morphology of In-doped SnS nanostructures showed that the In-dopant had been doped successfully in SnS lattice.

3.2. Crystallite size and strain

In this section, different methods were used to calculate the crystallite size and the lattice strain. These methods are Scherrer's method, W–H method (including UDM, UDSM, and UDEDM), and SSP method.

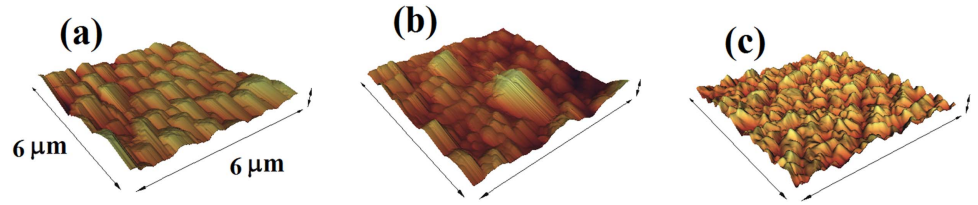

Figure 4. AFM images of, (a) I (0), (b) I (1), and (c) I (2) samples.

3.2.1. Scherrer's method

Using XRD patterns, the crystallite size (D) is estimated from Scherrer's equation [31, 32],

$$D = \frac{K\lambda}{\beta_{hkl}\cos\theta_B} \tag{3}$$

where D, K, and λ are the crystallite size, shape-dependent constant equal 0.94, and the X-ray wavelength of Cu-K_α radiation (0.154 056 nm), respectively. Also, β_{hkl} is the peak width at half maximum intensity (FWHM), and θ_B is the Bragg's angle. The width of the Bragg's angle is formed by the mixture of the instrumental- and the sample-dependent effects.

The instrumental effect is evaluated from the peak broadening of a reference sample (silicon). Therefore, considering the instrumental effect, β_{hkl} can be obtained as follows [31],

$$\beta_{hkl} = \sqrt{\beta^2{}_{hkl}(measured) - \beta^2{}_{hkl}(instrumental)} \tag{4}$$

Scherrer's equation can be rearranged by applying the corrected β_{hkl} as follows,

$$D = \frac{k\lambda}{\beta_{hkl}\cos\theta} \Rightarrow \cos\theta = \frac{k\lambda}{D}\left(\frac{1}{\beta_{hkl}}\right) \tag{5}$$

The crystallite size (D) is estimated from the slope of $\cos\theta$ versus $1/\beta_{hkl}$ plot using equation (5). Consequently, the value of $k\lambda$/slope shows the crystallite size value. Figure 5 depicts Scherrer's plots of undoped- and nanostructured In-doped SnS thin films. It is clear that the crystallite size D of SnS reduced due to In-doping. Also, the decrease in D of undoped SnS thin films after In-doping can be due to the change in effective ionic radii of Sn^{2+} and In^{3+}. Therefore, the crystalline quality of undoped SnS has been decreased after In-doping, which it could be attributed to the created lattice mismatch.

3.2.2. W–H methods

The Williamson-Hall (W–H) and size-strain plot (SSP) are two methods to estimate the D and lattice strain. In this paper, three models of a W–H method including UDM, UDSM, and UDEDM have been used to estimate the structural parameters. UDM model proposed to examine the uniform strain in the crystalline lattices. In this method, the W–H formula relies on the size broadening effect and strain broadening effect. The size broadening effect is described with Debye-Scherer (β_{DS}) formula (equation (3)), while the strain broadening term originated from defects and distortion in crystal lattices (equation (6)).

$$\beta_\varepsilon = C\,\varepsilon\tan\theta \tag{6}$$

In the above equation, ε is a maximum tensile or compressive strain, and C is a constant that assumed as 4. The above relation originated from the differential of the Bragg equation ($n\lambda = 2d\sin\theta_B$) concerning the d-spacing and the diffraction angle. According to the lattice strain is considered as $\Delta d/d = 2\varepsilon$, the strain-inducing term is obtained as follows [33],

$$\left|\frac{\Delta d}{d}\right| = \cot\theta\Delta\theta \Rightarrow \Delta(2\theta) = 2\left|\frac{\Delta d}{d}\right| \tan\theta = 4\varepsilon\tan\theta \tag{7}$$

In order to $\beta_{hkl} = \beta_\varepsilon + \beta_{DS}$, the equation (8) obtained as follows [34],

$$\beta_{hkl} = \frac{k\lambda}{D.\cos\theta_B} + 4\varepsilon.\tan\theta \tag{8}$$

By rearranging the above equation, the W–H relation (equation (9)) is obtained [31].

$$\beta_{hkl}.\cos\theta_B = \frac{k\lambda}{D} + 4\varepsilon.\sin\theta \tag{9}$$

According to equation (9), the D and ε can be achieved. The values of y-intercept (at $\beta_{hkl}.\cos\theta = 0$) and the slope of the $\beta_{hkl}.\cos\theta$ versus 4 $\sin\theta$ plot showed $k\lambda/D$ *and* ε and, respectively. The W–H diagrams of pure SnS

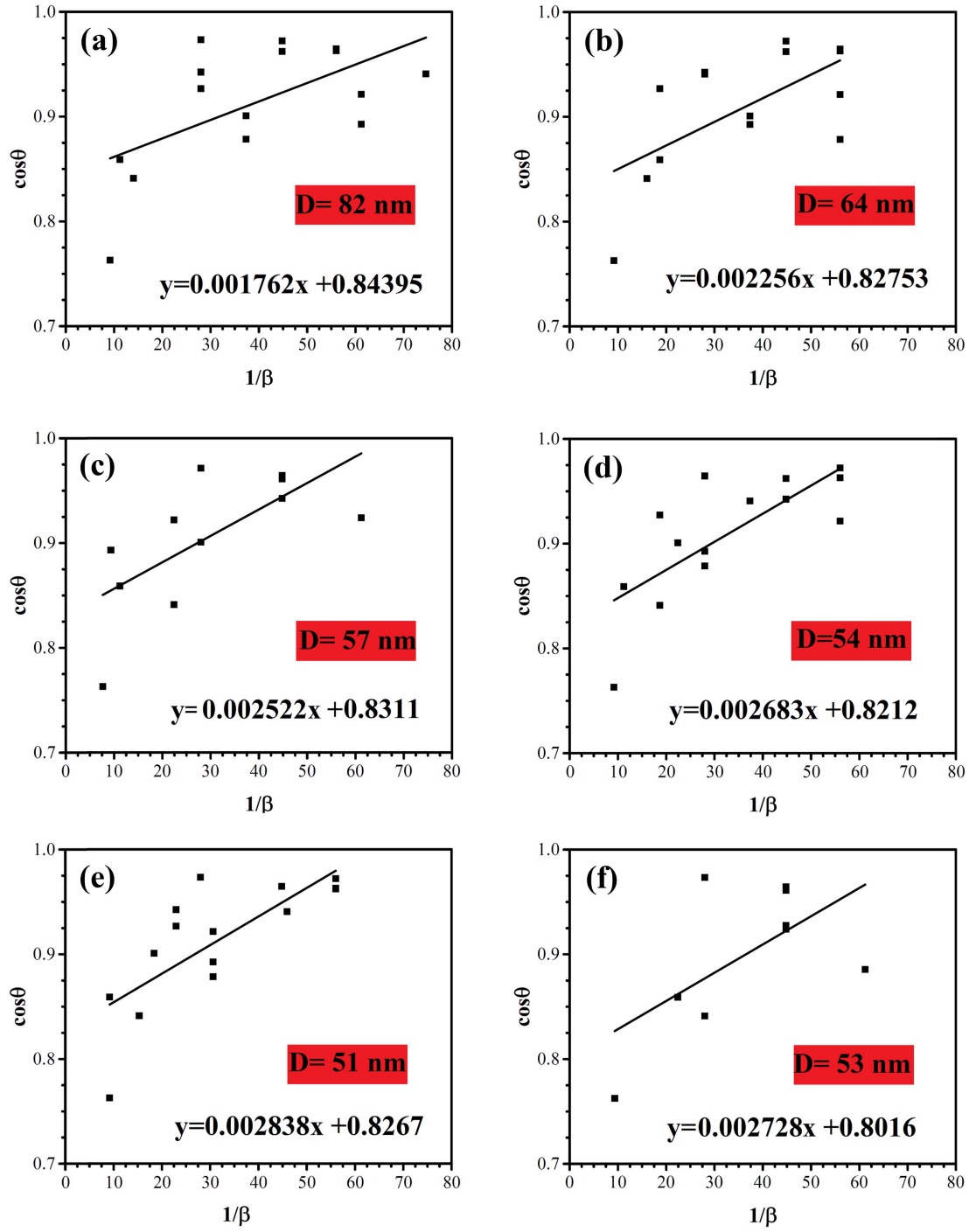

Figure 5. Scherrer's plots of pure SnS and nanostructured In-doped SnS thin films, the crystallite size *D* extracted from the slope of the fit.

and In-doped SnS thin films are shown in figure 6. As shown in this figure, because of the difference in the effective ionic radii of Sn^{2+} ions and In^{3+} ions, by increasing the amount of In-dopant in the SnS structure, the D and ε of In-doped SnS samples decreased and increased, respectively.

According to the elastic modulus of materials shows anisotropic nature, the microstrain is not constant in all crystallographic directions. Therefore, considering the anisotropic nature of Young's modulus, the UDSM and UDEDM methods have been used to measure structural characterizations of crystalline lattices. In the UDSM model, it is supposed that the lattice stress (σ) is identical in all crystallographic directions. Therefore, the anisotropic behavior of the elastic modulus of materials is responsible for the anisotropic performance of micro-strain (ε_{hkl}) and energy density (u) [35]. As we know, in the elastic deformation zone, the Hooke's law is usable. According to the Hooke's law, the σ and ε have linear variations to each other. Therefore, the stress is obtained by using $\sigma = \varepsilon E_{hkl}$ formula, which σ, ε, and E_{hkl} are lattice stress, lattice strain, and elastic modulus in the

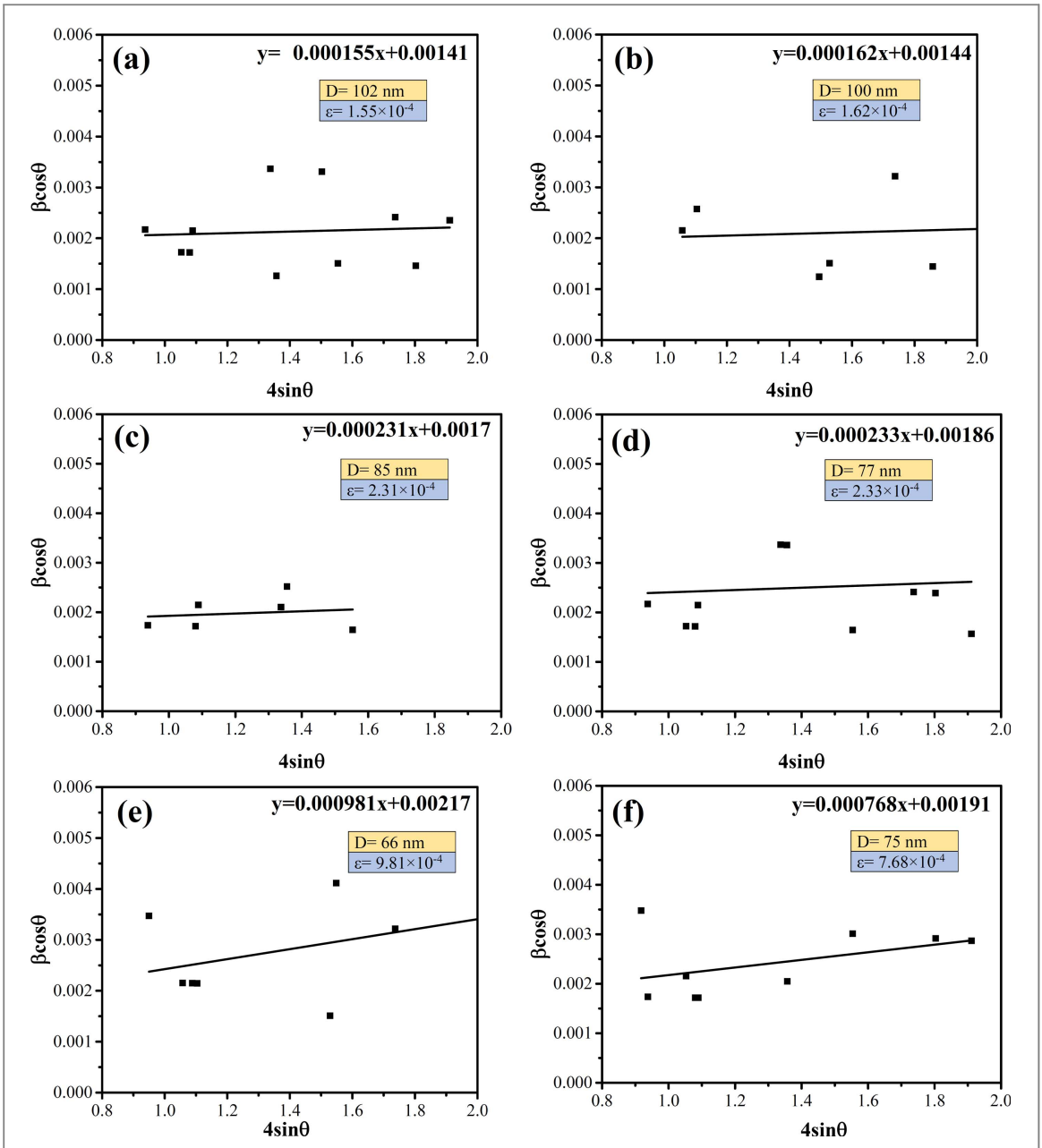

Figure 6. The UDM Williamson-Hall plots for nanostructured pure SnS and In-doped SnS thin films.

vertical direction to the crystalline planes (hkl) crystalline lattices, respectively. Therefore, the equation (9) modified by putting the value of $\varepsilon = \sigma/E_{\text{hkl}}$ as follows,

$$\beta_{hkl}.\cos\theta_B = \frac{k\lambda}{D} + \frac{4.\sin\theta}{E_{hkl}}\sigma \tag{10}$$

According to the above equation, the UDSM plot has been drawn by considering $\beta\cos\theta$ versus $4\sin\theta/E_{\text{hkl}}$. Therefore, the D and the ε are estimated from the y-intercept and the slope of this plot, respectively. Young's modulus in the orthorhombic structures obtained as follows, [36],

$$\frac{1}{Y_{hkl}} = l_1^4 s_{11} + 2l_1^2 l_2^2 s_{12} + 2l_1^2 l_3^2 s_{13} + l_2^4 s_{22} + 2l_2^2 l_3^2 s_{23} + l_3^4 s_{33} + l_2^2 l_3^2 s_{44} + l_1^2 l_3^2 s_{55} + l_1^2 l_2^2 s_{66} \tag{11}$$

where l_i is the unit vector for a particular (hkl) plane and s_{11}, s_{12}, s_{13}, s_{22}, s_{23}, s_{33}, s_{44}, s_{55}, and s_{66} were the elastic compliance of SnS with values of 11.92, −2.93, −4.32, 10.07, −8.2, 19.08, 19.46, 35.8, and 35.27 $(\text{TPa})^{-1}$, respectively. Figure 7 shows the UDSM plots for pure SnS and In-doped SnS thin films.

The above results showed that an increase in the amount of In-doping in SnS lattice results in a decrease and an increase in D and ε, respectively. Therefore, it can be said that the micro tensile stress in the In-doped SnS thin films may be due to the creation of grain boundaries [34].

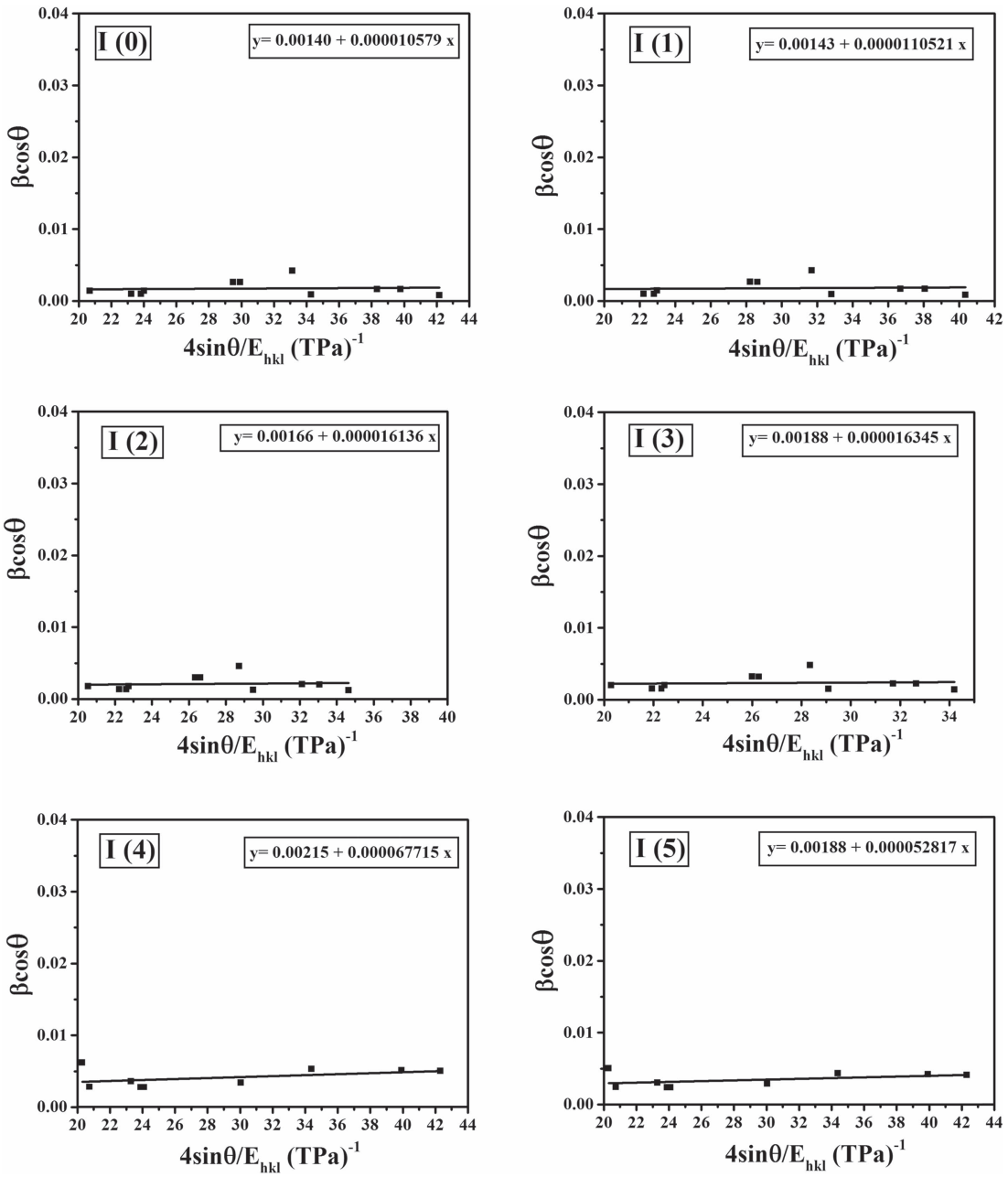

Figure 7. UDSM plots of pure SnS and In-doped SnS thin films.

The other form of W–H method is UDEDM. In this method, the energy density (u) is assumed unchanging in all crystallographic directions, while the deformation stress (σ) is presumed anisotropic [35]. Considering the Hooke's law in the elastic deformation zone, the energy density (u) defines as $u = \varepsilon^2 E_{\mathrm{hkl}}/2$. Therefore, the UDEDM formula is obtained by rearranging the equation (9),

$$\beta_{hkl} \cos\theta = k\lambda/D + \left(\frac{4\sin\theta}{(Y_{hkl}/2)^{1/2}}\right) \times u^{\frac{1}{2}} \tag{12}$$

The UDEDM graphs have been plotted to estimate the D and u. The UDEDM curves are drawn with $\beta\cos\theta$ against $4\sin\theta/(Y_{\mathrm{hkl}}/2)^{1/2}$. The UDEDM graphs of pure SnS and In-doped SnS thin films showed in figure 8. It was evident in the equation (12) that the D and u are estimated by the y-intercept and slope of the fit, respectively. Based on equation (12), the D and u are calculated using the below equation.

$$D = \frac{0.1448}{y-\text{intercept}}(\text{nm})$$
$$u = (slope)^2 \tag{13}$$

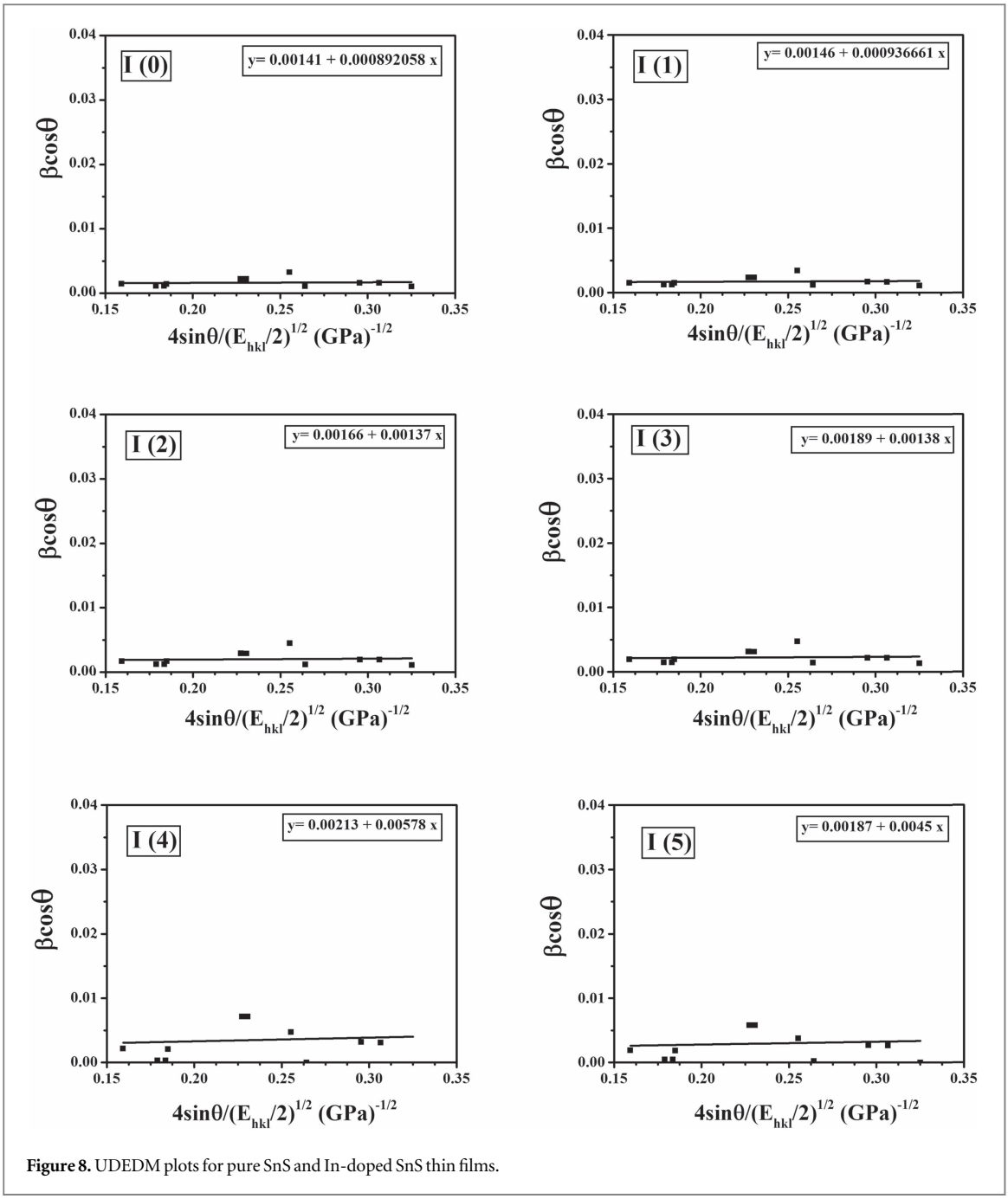

Figure 8. UDEDM plots for pure SnS and In-doped SnS thin films.

According to UDEDM model, the *D* and *u* of undoped SnS are decreased and increased, respectively, after In-doping. As previously described, introduction an In^{3+} ion with different effective ionic radii compared with Sn^{2+} in SnS lattice leads to create mismatch and imperfection in SnS lattice. Therefore, it increased the energy density in In-doped SnS crystalline lattice. According to Hooke's law, an increase in energy density increases the lattice stress and lattice strain.

The calculated *D* values from W–H methods including UDM, UDSM, and UDEDM are well matched to each other. These are because the presence of strain in various models of W–H analysis has a minimal influence on the average *D* of SnS thin films. Also, the value of average crystallite size of un- and In-doped SnS samples estimated from Scherrer's method and W–H analysis shows a deviation, which this is due to (i) strain broadening effect and (ii) the change in averaging the distribution of particle size [27]. Similar results were observed in [31].

3.2.3. SSP method

Size strain plot (SSP) technique is another suitable method to investigate the *D* and ε. In this method, the nature of the crystals considered isotropic [37]. In addition, the crystallite size profile and the strain profile defined by the Lorentzian and the Gaussian function, respectively [26]. According to the SSP method, the following

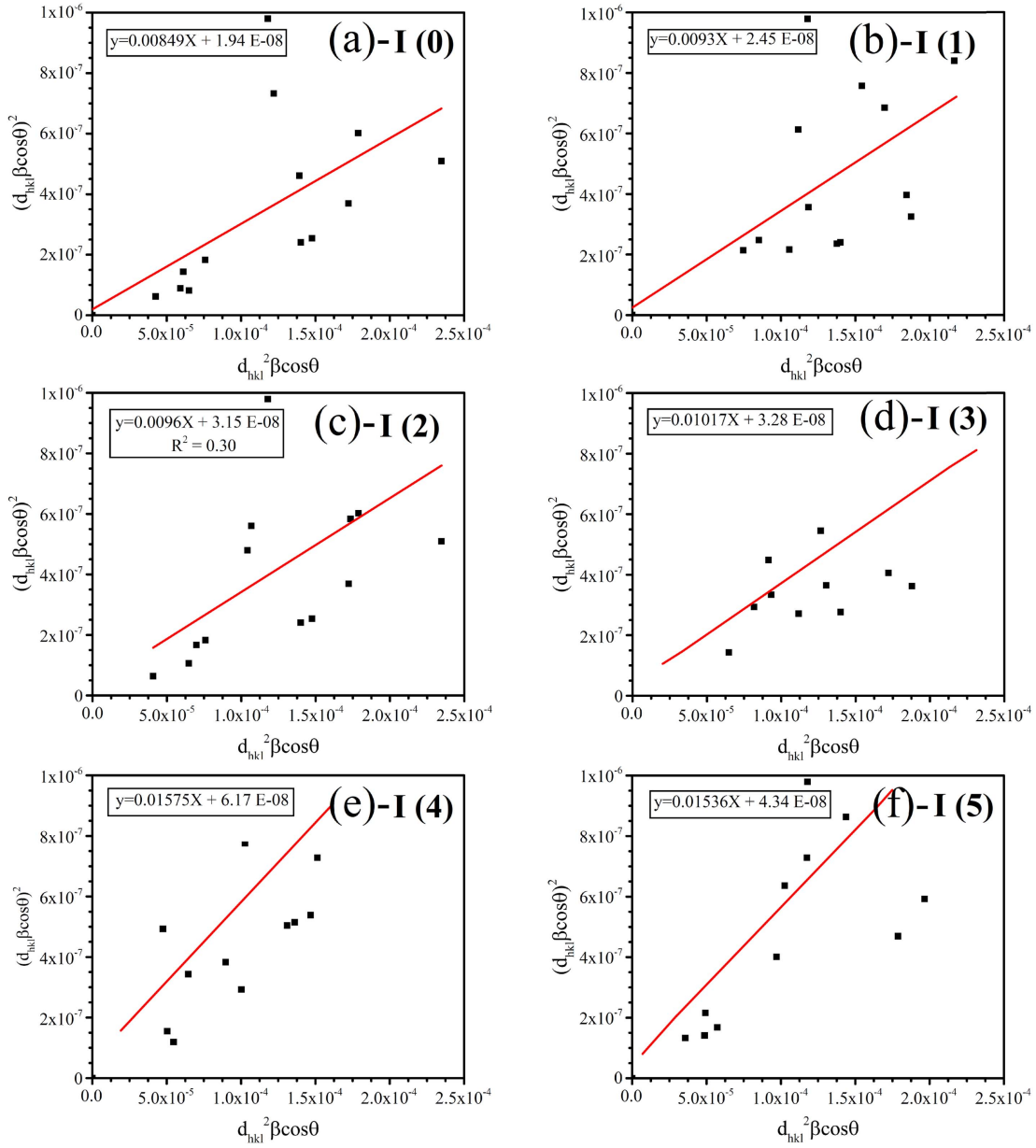

Figure 9. Size strain plots (SSP) for pure SnS and In-doped SnS thin films.

equation is employed to describe the relation between the ε and D [38],

$$(\beta_{hkl}.\cos\theta.d_{hkl})^2 = \frac{A}{D}(d_{hkl}^2.\beta_{hkl}.\cos\theta) + \left(\frac{\varepsilon}{2}\right)^2 \quad (14)$$

where A is a constant which equals ¾ for spherical particles. By plotting $(\beta_{hkl}.\cos\theta.d_{hkl})^2$ versus $d_{hkl}^2.\beta_{hkl}.\cos\theta$ as displayed in figure 9 (SSP plot), the D and ε of undoped- and In-doped SnS thin films can be achieved. According to figure 9 and equation (14), the D and the ε can be obtained from the slope and y-intercept (in which $(\beta_{hkl}.\cos\theta.d_{hkl})^2 = 0$), respectively. The extracted results from Scherrer's method, W–H method, and SSP method listed in table 2. In addition, the obtained values of D and ε for pure SnS and In-doped SnS thin films using Scherrer's-, W–H- and SSP methods are compared in figure 10. As shown in figure 10, with the increase of the amount of In-dopant in the SnS lattice, the D decreased and subsequently, the ε increased. It is due to the fact that with introducing the indium ions into SnS lattice, the lattice has been accompanied by mismatches related to different effective ionic radii of In^{3+} and Sn^{2+} ions. The results showed that the obtained D from Scherrer's method is less than that of W–H and SSP method. It can occur due to the impact of ε which reflects the importance of the lattice strain [39]. Consequently, it can be said that there is good accordance between structural parameters obtained from UDEDM, UDM, UDSM models, SSP method, and the results of the Scherrer's formula and TEM image.

Table 2. Structural parameters for un- and In-doped SnS thin films using Scherrer's, W–H, and SSP methods.

		Williamson-Hall method											
	Scherrer's method	UDM		UDSM			UDEDM				Size-Strain plot method			
Sample	D (nm)	D (nm)	$\varepsilon \times 10^{-4}$	D (nm)	$\varepsilon \times 10^{-4}$	σ (MPa)	D (nm)	$\varepsilon \times 10^{-4}$	σ (MPa)	U (Kjm^{-3})	D (nm)	$\varepsilon \times 10^{-4}$	σ (MPa)	U (Kjm^{-3})
I (0)	82	102	1.55	103.4	1.53	10.57	102.6	1.51	10.43	0.78	88.3	2.79	19.28	2.69
I (1)	64	100	1.62	101.2	1.59	10.99	99.1	1.59	10.99	0.87	80.6	3.13	21.63	3.38
I (2)	57	85	2.31	87.2	2.33	16.10	87.2	2.33	16.10	1.87	78.1	3.53	24.39	4.30
I (3)	54	77	2.33	77.0	2.36	16.31	76.6	2.34	16.17	1.89	73.7	3.62	25.02	4.52
I (4)	51	66	9.81	67.3	9.79	62.00	67.9	9.83	67.94	33.39	47.6	4.97	34.35	8.53
I (5)	53	75	7.68	77.0	7.64	47.51	77.4	7.65	52.87	20.22	48.8	4.17	28.82	6.00

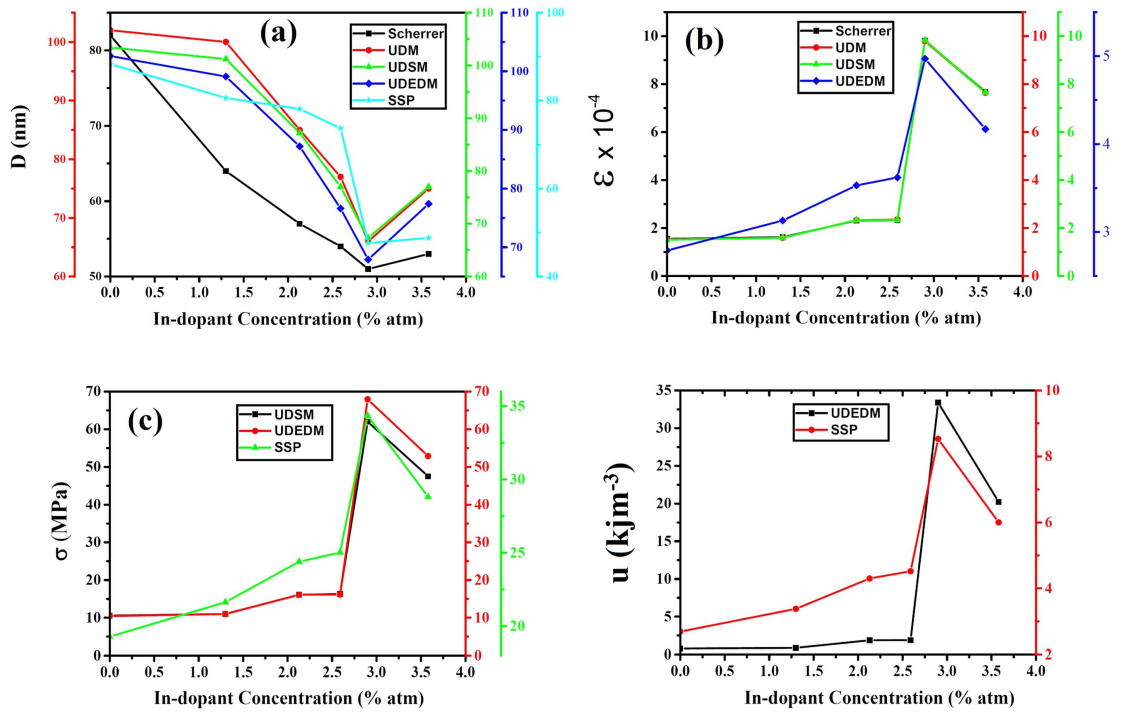

Figure 10. Comparison between the structural parameters of pure SnS and In-doped SnS samples obtained using different methods, (a) crystallite size D, (b) lattice strain ε, (c) lattice stress σ, and (d) energy density (u).

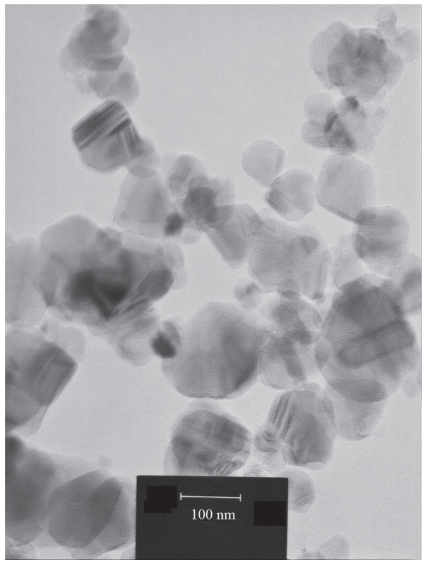

Figure 11. TEM image of undoped SnS sample.

3.2.4. TEM method

To discover the reality of obtained data from XRD analysis, TEM analysis was applied. TEM is an excellent analysis to examine the size and the shape of deposited SnS. The TEM image for pure SnS thin films is shown in figure 11. It is evident in TEM image that the average particle size is in good accordance with the average D assessed by the W–H and SSP techniques.

3.3. PL

PL is a non-destructive test for examination the crystalline quality of materials. PL spectra can confirm XRD measurements. The room temperature PL spectra of pure SnS and In-doped SnS thin films are presented in figure 12. The photo-excitation wavelength was 350 nm. As it is evident in this figure, two emission peaks

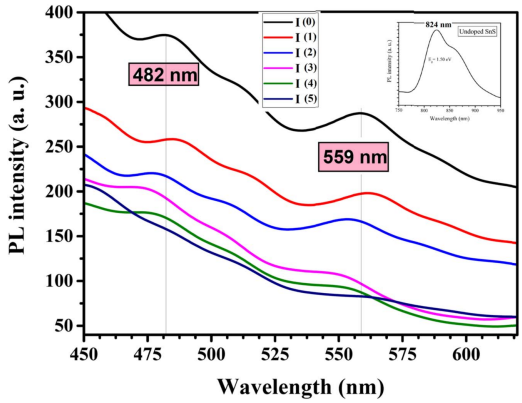

Figure 12. PL spectra of nanostructured pure and In-doped SnS thin films with an excitation wavelength of 350 nm (3.54 eV).

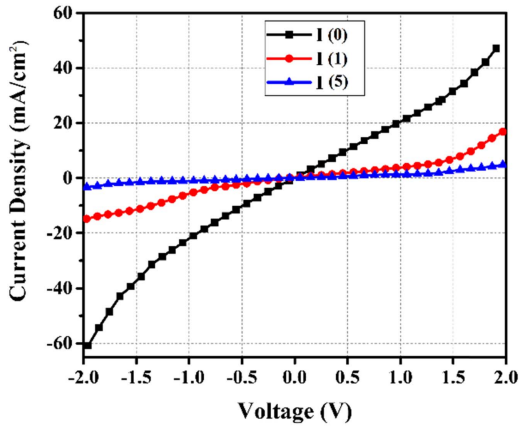

Figure 13. I-V characteristics of undoped SnS and In-doped SnS thin films.

containing a blue emission peak at 482 nm and a green emission peak at 559 nm observed for all samples. Thus, the In-doped SnS thin films used as blue and/or green emitters or other devices owing to blue and green emission bands. Based on our investigations, these emission bands can occur due to the high density of sulfur, tin vacancies, tin interstitials, and stacking faults [40, 41]. Liu *et al* observed two peaks at 365 nm and 464 nm for SnO_2 nanoparticles that the peak at 464 nm is related to oxygen vacancies [42]. The observed blue emission peak is similar to that reported in [40, 43], and the green emission is similar to that studied in Ref. [44]. As shown in the inset, the band-to-band emission of SnS was seen at ~824 nm ($E_g = 1.5$ eV). As it is obvious in figure 12, compared to the pure SnS thin film, the PL intensity of In-doped SnS samples decreased that it showed the crystalline quality of In-doped SnS is decreased. This observance is in good accordance with XRD patterns.

3.4. Electrical properties

In order to investigate the effect of structural properties on the electrical behaviors of SnS thin films, the voltage-current (I-V) curves (figure 13) of undoped SnS and In-doped SnS thin films have been drawn under ambient condition.

A Schottky behavior in the voltage-current characteristic was observed for all samples. According to figure 13, by adding In concentration in SnS lattice, at a same voltage we have lower current, which this means an increase in the electrical resistivity of SnS thin films. As shown in the XRD results, the crystalline quality of SnS thin films has been decreased after In-doping. Also, the dislocation density, grain boundaries, lattice strain, and lattice stress of In-doped SnS thin films have been increased compared to the undoped SnS thin films. Therefore, the transportation of electrical carrier became more difficult in SnS lattice due to In-doping. Consequently, the results of I-V curve confirmed the results of XRD analysis.

4. Conclusion

Six deposited samples containing pure SnS and In-doped SnS thin films synthesized by an electrodeposition method on the FTO substrates. The results of XRD patterns clearly showed that all of the deposited thin films were orthorhombic polycrystalline. In this research, the line broadening investigations on pure SnS and In-doped SnS thin films have been investigated. Therefore, the Scherrer's method, modified forms of W–H (UDM) method, and the SSP method have been used to analyze the line broadening of pure SnS and In-doped SnS (with different concentration of In-dopant) samples. The results obtained by these methods showed that an increase in the amount of In-dopant in SnS lattice leads to a reduction in the crystallite size and an increase in the lattice strain. There were happened due to the variation in the effective ionic radii of In^{3+} and Sn^{2+} ions. Therefore, substitution of In^{3+} for Sn^{2+} in the SnS lattice leads to creates mismatches in the SnS crystal lattice. This lattice mismatch is responsible for the reduction of the crystalline quality and the increase in lattice strain. In addition, the result of TEM image confirms our obtained results.

ORCID iDs

Hosein Kafashan https://orcid.org/0000-0003-2031-4261

References

[1] Kois J, Bereznev S, Maricheva J and Revathi N 2017 Electrochemical and photoelectrochemical characterization of SnS photoabsorber films *Materials Science in Semiconductor Processing* **58** 76–81
[2] Fang Z, Wang Q, Wang X, Fan F, Wang C and Zhang X 2013 Uniform hierarchical SnS microspheres: solvothermal synthesis and lithium ion storage performance *Mater. Res. Bull.* **48** 4935–41
[3] Zhu J, Wang D and Liu T 2013 Preparation of tin sulfide–graphene composites with enhanced lithium storage *Appl. Surf. Sci.* **282** 947–53
[4] Tao H-C, Yang X-L, Zhang L-L and Ni S-B 2014 One-step *in situ* synthesis of SnS/graphene nanocomposite with enhanced electrochemical performance for lithium ion batteries *J. Electroanal. Chem.* **728** 134–9
[5] Lefebvre I, Lannoo M, Moubtassim M E, Fourcade J O and Jumas J-C 1997 Lithium insertion in three-dimensional tin sulfides *Chem. Mater.* **9** 2805–14
[6] Manukumar K N, Nagaraju G, Kishore B, Madhu C and Munichandraiah N 2018 Ionic liquid-assisted hydrothermal synthesis of SnS nanoparticles: electrode materials for lithium batteries, photoluminescence and photocatalytic activities *Journal of Energy Chemistry* **27** 806–12
[7] Li K, Yan S, Lin Z and Shi Y 2016 Facile solution synthesis of tin sulfide nanobelts for lithium-ion batteries *J. Alloys Compd.* **681** 486–91
[8] Lu L, Zhang L, Zeng H, Xu B, Wang L and Li Y 2017 Enhanced cycling performance of Se-doped SnS carbon nanofibers as negative electrode for lithium-ion batteries *J. Alloys Compd.* **695** 1294–300
[9] Kang J-Y, Kwon S-M, Yang S H, Cha J-H, Bae J A and Jeon C-W 2017 Control of the microstructure of SnS photovoltaic absorber using a seed layer and its impact on the solar cell performance *J. Alloys Compd.* **711** 294–9
[10] Kabiri Samani N, Dehghani Tafti Z, Bioki H A, Zarandi M B and Shayegh S 2017 Annealing effect on structural and optical constants of SnS thin films for solar cells application *Optik—International Journal for Light and Electron Optics* **131** 231–41
[11] Kafashan H, Azizeh M and Balak Z 2017 Electrochemical synthesis of nanostructured Se-doped SnS: Effect of Se-dopant on surface characterization *Appl. Surf. Sci.* **410** 186–95
[12] Andrade-Arvizu J A, García-Sánchez M F, Courel-Piedrahita M, Pulgarín-Agudelo F, Santiago-Jaimes E, Valencia-Resendiz E, Arce-Plaza A and Vigil-Galán O 2016 Suited growth parameters inducing type of conductivity conversions on chemical spray pyrolysis synthesized SnS thin films *Journal of Analytical and Applied Pyrolysis* **121** 347–59
[13] Ninan G G, Kartha C S and Vijayakumar K P 2016 Spray pyrolysed SnS thin films in n and p type: optimization of deposition process and characterization of samples *Journal of Analytical and Applied Pyrolysis* **120** 121–5
[14] Polivtseva S, Katerski A, Kärber E, Oja Acik I, Mere A, Mikli V and Krunks M 2017 Post-deposition thermal treatment of sprayed SnS films *Thin Solid Films* **633** 179–84
[15] Wang W, Leung K, Fong W, Wang S, Hui Y, Lau S, Chen Z, Shi L, Cao C and Surya C 2012 Molecular beam epitaxy growth of high quality p-doped SnS van der Waals epitaxy on a graphene buffer layer *J. Appl. Phys.* **111** 093520
[16] Ali S, Wang F, Zubair Iqbal M, Ullah Shah H and Zafar S 2017 Hydrothermal synthesis, characterization and optical properties of SnS prismatic nanorods *Mater. Lett.* **206** 22–5
[17] Reghima M, Akkari A, Guasch C, Castagné M and Kamoun-Turki N 2013 Synthesis and characterization of Fe-doped SnS thin films by chemical bath deposition technique for solar cells applications *Journal of Renewable and Sustainable Energy* **5** 063109
[18] Reghima M, Akkari A, Guasch C and Kamoun-Turki N 2012 Effect of indium doping on physical properties of nanocrystallized SnS zinc blend thin films grown by chemical bath deposition *Journal of Renewable and Sustainable Energy* **4** 011602
[19] Akkari A, Reghima M, Guasch C and Kamoun-Turki N 2012 Effect of copper doping on physical properties of nanocrystallized SnS zinc blend thin films grown by chemical bath deposition *J. Mater. Sci.* **47** 1365–71
[20] Jing J, Cao M, Wu C, Huang J, Lai J, Sun Y, Wang L and Shen Y 2017 Chemical bath deposition of SnS nanosheet thin films for FTO/SnS/CdS/Pt photocathode *J. Alloys Compd.* **726** 720–8
[21] Gedi S, Reddy V R M, Kang J-Y and Jeon C-W 2017 Impact of high temperature and short period annealing on SnS films deposited by E-beam evaporation *Appl. Surf. Sci.* **402** 463–8
[22] Henry J, Mohanraj K, Kannan S, Barathan S and Sivakumar G 2013 Effect of selenium doping on structural and optical properties of SnS: se thin films by electron beam evaporation method *The European Physical Journal-Applied Physics* **61** 10301
[23] Tsukigase H, Suzuki Y, Berger M-H, Sagawa T and Yoshikawa S 2011 Synthesis of SnS nanoparticles by SILAR method for quantum dot-sensitized solar cells *J. Nanosci. Nanotechnol.* **11** 1914–22

[24] Kafashan H, Azizeh M and Nasri Vatan H 2016 Ultrasound-assisted electrodeposition of SnS: Effect of ultrasound waves on the physical properties of nanostructured SnS thin films *J. Alloys Compounds* **686** 962–8
[25] Kafashan H, Jamali-Sheini F, Ebrahimi-Kahrizsangi R and Yousefi R 2016 Influence of growth conditions on the electrochemical synthesis of SnS thin films and their optical properties *Int. J. Miner. Metall. Mater.* **23** 348–57
[26] Sivakami R, Dhanuskodi S and Karvembu R 2016 Estimation of lattice strain in nanocrystalline RuO2 by Williamson–Hall and size–strain plot methods *Spectrochimica Acta Part A: Molecular and Biomolecular Spectroscopy* **152** 43–50
[27] Yogamalar R, Srinivasan R, Vinu A, Ariga K and Bose A C 2009 X-ray peak broadening analysis in ZnO nanoparticles *Solid State Commun.* **149** 1919–23
[28] Kafashan H, Jamali-Sheini F, Azizeh M, Balak Z, Cheraghizade M and Nasiri Vatan H 2017 Electrochemical deposition of nanostructured $SnS_{1-x}Te_x$ thin films and their surface characterization *J. Alloys Compunds* **694** 1338–47
[29] Kafashan H and Balak Z 2017 Preparation and characterization of electrodeposited SnS: in thin films: effect of In dopant *Spectrochimica Acta Part A: Molecular and Biomolecular Spectroscopy* **184** 151–62
[30] Kafashan H, Ebrahimi-Kahrizsangi R, Jamali-Sheini F and Yousefi R 2016 Effect of Al doping on the structural and optical properties of electrodeposited SnS thin films *Physica Status Solidi* (a) **213** 1302–8
[31] Aly K A, Khalil N M, Algamal Y and Saleem Q M A 2016 Lattice strain estimation for $CoAl_2O_4$ nano particles using Williamson-Hall analysis *J. Alloys Compd.* **676** 606–12
[32] Kafashan H, Jamali-Sheini F, Ebrahimi-Kahrizsangi R, Yousefi R and Jeon C-W 2016 Nanostructured $SnS_{1-x}Te_x$ thin films: Effect of Te concentration and physical properties *J. Alloys Compounds* **681** 595–605
[33] Burton A W, Ong K, Rea T and Chan I Y 2009 On the estimation of average crystallite size of zeolites from the Scherrer equation: a critical evaluation of its application to zeolites with one-dimensional pore systems *Microporous and Mesoporous Materials* **117** 75–90
[34] Thandavan T M K, Gani S M A, San Wong C and Nor R M 2015 Evaluation of Williamson–Hall strain and stress distribution in ZnO nanowires prepared using aliphatic alcohol *J. Nondestruct. Eval.* **34** 14
[35] Madhu G, Bose V C, Maniammal K, Aiswarya Raj A S and Biju V 2013 Microstrain in nanostructured nickel oxide studied using isotropic and anisotropic models *Physica B: Condensed Matter* **421** 87–91
[36] Nye J F 1985 *Physical Properties of Crystals: their Representation by Tensors and Matrices* (Oxford: Oxford University Press)
[37] Khorsand Zak A, Yousefi R, Majid W H A and Muhamad M R 2012 Facile synthesis and x-ray peak broadening studies of Zn1−xMgxO nanoparticles *Ceram. Int.* **38** 2059–64
[38] Yousefi R, Zak A K and Jamali-Sheini F 2013 Growth, x-ray peak broadening studies, and optical properties of Mg-doped ZnO nanoparticles *Materials Science in Semiconductor Processing* **16** 771–7
[39] Khorsand Zak A, Majid W H A, Ebrahimizadeh Abrishami M, Yousefi R and Parvizi R 2012 Synthesis, magnetic properties and x-ray analysis of Zn0.97X0.03O nanoparticles (X = Mn, Ni, and Co) using Scherrer and size–strain plot methods *Solid State Sciences* **14** 488–94
[40] Zhao Y, Zhang Z, Dang H and Liu W 2004 Synthesis of tin sulfide nanoparticles by a modified solution dispersion method *Materials Science and Engineering:* B **113** 175–8
[41] Sohila S, Rajalakshmi M, Muthamizhchelvan C, Kalavathi S, Ghosh C, Divakar R, Venkiteswaran C N, Muralidharan N G, Arora A K and Mohandas E 2011 Synthesis and characterization of SnS nanosheets through simple chemical route *Mater. Lett.* **65** 1148–50
[42] Liu J and Xue D 2010 Sn-based nanomaterials converted from SnS nanobelts: facile synthesis, characterizations, optical properties and energy storage performances *Electrochim. Acta* **56** 243–50
[43] Yue G, Lin Y, Wen X, Wang L, Chen Y and Peng D 2012 Synthesis and characterization of the SnS nanowires via chemical vapor deposition *Appl. Phys.* A **106** 87–91
[44] Devika M, Koteeswara Reddy N, Prashantha M, Ramesh K, Venkatramana Reddy S, Hahn Y and Gunasekhar K 2010 The physical properties of SnS films grown on lattice-matched and amorphous substrates *Phys. Status Solidi* (a) **207** 1864–9